AIAA JOURNAL
Vol. 40, No. 6, June 2002

Large Eddy Simulation of Flow Around an Airfoil Near Stall

Ivan Mary* and Pierre Sagaut*
ONERA, 92322 Châtillon, France

A large eddy simulation (LES) of a turbulent flow past an airfoil near stall at a chord Reynolds number of 2.1×10^6 is performed and compared with wind-tunnel experiments. This configuration still constitutes a challenging test case for Reynolds-averaged Navier–Stokes (RANS) simulation and LES as a result of the complexity of the suction side boundary layer: an adverse pressure gradient creates successively a laminar separation bubble, a turbulent reattachment, and a turbulent separation near the trailing edge. To handle this high-Reynolds-number flow with LES on available supercomputers, a local mesh-refinement technique and a discretization of the convective fluxes are developed in a block-structured finite volume code to reduce the total number of grid points and the numerical dissipation acting on the small scales, respectively. Influence of subgrid scale modeling (SGS) is assessed through the comparisons of explicit selective mixed scale model (SMSM) and implicit monotone-integrated LES model results. Moreover, the solution sensitiveness to grid refinement and spanwise extent is investigated. With the use of the largest grid (7.2×10^6 cells) and SMSM model, the computed mean and fluctuating velocity profiles compare favorably with experimental measurements, which constitute to the authors' knowledge the first satisfying LES of this complex flow.

Nomenclature

c	=	airfoil chord
M_0	=	Mach number
Pr	=	Prandtl number
Q_c	=	conservative variables
Re	=	Reynolds number
γ	=	specific heat ratio
δ_{ij}	=	Kronecker tensor
ϕ_{rms}	=	rms quantity

Subscripts

0	=	reference quantity
∞	=	upstream condition

Introduction

LARGE eddy simulations (LES) and direct simulations have been successfully used over the last decade to study turbulent academic flows, leading to significant improvements of both numerical methods and subgrid scale (SGS) models. These successes have raised the interest of the aeronautical industry, for which LES appears as a potential tool for some specific applications. For instance, the simulation of the flow over a high-lift multielements airfoil in landing configuration offers a practical industrial interest for the prediction of the radiated noise because LES can provide accurate description of the acoustic sources.[1,2] However, the use of LES for such application remains a challenging task for the computational fluid dynamics (CFD) community: the high value of the Reynolds number ($Re \geq 10^6$) and the complexity of the different turbulent boundary layers (including transitional phenomena and separations) still render this simulation unaffordable. Therefore recent works of several researchers[3–5] have been dedicated to the simulation of two-dimensional isolated profiles, which represents a first step toward the real configuration. But even for this simpler case, the accuracy of their different results was not satisfactory, which underlines the current limitations of LES. On the one hand, computational capacity of available supercomputers does not allow use of the mesh resolution usually required by LES of wall bounded flow. If $\boldsymbol{x}$, $\boldsymbol{y}$, and $\boldsymbol{z}$ represent the streamwise, wall normal, and spanwise directions respectively, then the following mesh resolution expressed in wall unit must be satisfied: $\Delta x^+ \leq 50$, $\Delta y^+ \approx 2$, $\Delta z^+ \approx 20$. On the other hand, the stability of the simulation often requires the use of some numerical dissipation, which deteriorates the efficiency of the SGS modeling. Consequently, LES of flow around an isolated airfoil still demands an effort to improve the numerical techniques and evaluate the solution sensitiveness to numerical parameters, such as the SGS modeling and the grid resolution.

Different solutions can be retained to bypass the limited capacity of available supercomputers. A first way is to consider wall functions for LES, which can allow for some specific flow cases the use of coarser resolution (see Ref. 6 for a short review). But a recent numerical study [Davidson, L., Cokljat, D., Fröhlich, J., Leschziner, M., Mellen, C., and Rodi, W. (eds.), *LESFOIL: LES of Flow Around a High Lift Airfoil*, manuscript in preparation] concerning flow around high-lift isolated airfoil has confirmed that wall functions are unable to produce accurate solutions for such complex separated flows. A second way to limit the computational cost of LES relies on local mesh refinement. This technique reduces the required number of grid points for a simulation by adapting the mesh resolution to the local flow length scales. Unstructured meshes are a natural tool to get an efficient cells distribution, but they have not yet been applied to direct numerical simulation and LES very extensively because of their cost and the difficulty in achieving high order of accuracy. For structured meshes Kravchenko et al.[7] have demonstrated that local mesh refinement could be a promising tool to handle LES of complex flow. This implies at least some interpolations of the flow variables at the boundaries of noncoincident blocks. Moreover, if the boundary is located in a turbulent zone the different cutoff lengths associated with each block require an enrichment procedure to preserve the accuracy, leading to discontinuous interface values of the unsteady flow variables and SGS viscosities.[8,9] For the simulation of flow over infinite spanwise body, Pascarelli et al.[10] have proposed a simpler strategy to decrease the computational cost of the simulation by using different spanwise extents in the inner and outer boundary layer. Assuming flow periodicity, the inner block information is repeated several times to match the number of spanwise discretization points in the outer block. This approach alleviates the difficulties involved by interpolation and enrichement procedures because conforming blocks are used. However, this technique only allows at best a reduction of 30% of the total number of grid points.

The numerical dissipation of the discretization scheme is the second point that must be adressed to enhance accuracy of LES for

Received 28 February 2001; presented as Paper 2001-2559 at the 15th Computational Fluid Dynamics Conference, Anaheim, CA, 11–16 June 2001; revision received 28 December 2001; accepted for publication 30 December 2001.

*Scientist Engineer, 29 av. de la Division Leclerc.

flow over an isolated airfoil. Indeed for stability reasons the purely centered scheme cannot generally be applied to the convective fluxes, if complex flows are considered. Thus two main approaches have been investigated in the past decade to deal with the numerical dissipation. The monotone-integrated large eddy simulation (MiLES), introduced by Boris et al.,[11] privileges the robustness of the simulation by using a shock-capturing scheme for the discretization. In such a case no explicit SGS model is employed, and the energy transfer from the large scales to the small ones is achieved by the artificial dissipation of shock-capturing scheme. This approach is still the subject of controversy. Indeed encouraging results have been obtained for complex flows,[12] although Garnier et al.[13] have demonstrated for isotropic homogeneous turbulence flows that the energy transfer cannot be recovered accurately, even if high-order ENO shock-capturing schemes are used. The second strategy concerning the numerical dissipation relies on hybrid centered/upwind discretizations. In such case a sensor is introduced to achieve a local application of the upwind formula, which minimizes its damping effect on the small scales. For instance this approach has been used by Ducros et al.,[14] who developed a shock detector to sucessfully perform a shock/turbulence interaction.

In the present study carried out during the European LESFOIL project (manuscript in preparation), new numerical techniques are proposed in order to enhance the capability of LES to predict the flow around an isolated airfoil. Concerning local mesh refinement, a two-/three-dimensional coupling strategy has been developed. Indeed in such simulations, the flow is laminar and two-dimensional in a large part of the computational domain. Thus three-dimensional computation can be limited to a zone close to the airfoil where the flow is turbulent, whereas two-dimensional simulations are used for the far field (Fig. 1). This strategy, which does not affect the accuracy of the simulation as long as the two-/three-dimensional interface is located in regions where the flow is two-dimensional laminar or inviscid, allows the use of a mesh with LES resolution, while keeping the total number of grid points at a reasonable level. Moreover a special effort has been focused on the spatial discretization of the convective terms, leading to the development of a second-order-accurate hybrid centered/upwinding formula. The key point of the scheme is the use of a sensor, which allows the introduction of locally some numerical dissipation when spurious oscillation is detected on one of the primitive variables. Therefore, the effect of the SGS model is not affected by the numerical dissipation as long as odd-even decoupling is not detected in the flow solution.

The governing equations are presented in the next section, whereas the numerical method is described in the third section. The fourth section is devoted to the presentation of the test case and the results comparison. The solution sensitiveness to mesh refinement, spanwise extent, and SGS modeling is investigated. For the SGS modeling the possibilities and limitations of MiLES[11] and selective mixed scale model (SMSM)[15] are compared.

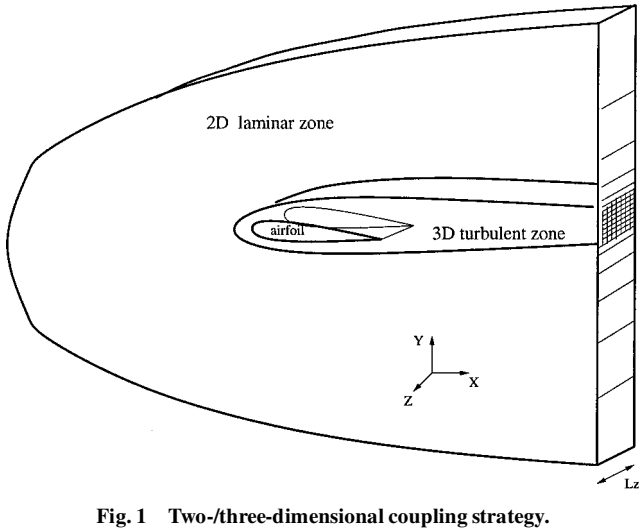

Fig. 1 Two-/three-dimensional coupling strategy.

Governing Equations

Filtered Navier–Stokes Equations

A dimensionless form of the three-dimensional unsteady filtered Navier–Stokes equations is used for a viscous compressible Newtonian fluid. Any flow variable ϕ can be written as $\phi = \bar{\phi} + \phi'$, where $\bar{\phi}$ represents the large-scale part of the variable and ϕ' its small-scale part. The filtering operator, classically defined as a convolution product on the computational domain, is assumed to commute with time and spatial derivatives. Moreover, it is convenient for the clarity of the equations to introduce the Favre filtering, $\tilde{\phi} = \overline{\rho\phi}/\bar{\rho}$. In conservative form the filtered Navier–Stokes equations can be expressed in three-dimensional Cartesian coordinates (x_1, x_2, x_3) as

$$\frac{\partial \bar{Q}_c}{\partial t} + \frac{\partial \bar{F}_j}{\partial x_j} - \frac{1}{Re}\frac{\partial \bar{F}_j^v}{\partial x_j} = 0 \tag{1}$$

The Reynolds number is defined as $Re = \rho_0 u_0 L_0/\mu_0$. The symbols u_0, ρ_0, L_0, and μ_0 denote a characteristic velocity, density, length, and dynamic viscosity, respectively. The conservative flow variables are defined as $\bar{Q}_c = [\bar{\rho}, \bar{\rho}\tilde{u}_1, \bar{\rho}\tilde{u}_2, \bar{\rho}\tilde{u}_3, \bar{p}/(\gamma-1) + \bar{\rho}\tilde{u}_j\tilde{u}_j/2]^t$ and the inviscid fluxes by $\bar{F}_j = \tilde{u}_j\bar{Q}_c + (0, \delta_{1j}\bar{p}, \delta_{2j}\bar{p}, \delta_{3j}\bar{p}, \bar{p}\tilde{u}_j)^t$. By using Boussinesq eddy viscosity hypothesis, the viscous fluxes are given by $\bar{F}_j^v = (0, \bar{\sigma}_{1j}, \bar{\sigma}_{2j}, \bar{\sigma}_{3j}, \bar{\sigma}_{kj}\tilde{u}_k + \hat{q}_j)^t$, with

$$\hat{\sigma}_{ij} = [\mu(\tilde{T}) + \mu_t]\left(\frac{\partial \tilde{u}_i}{\partial x_j} + \frac{\partial \tilde{u}_j}{\partial x_i} - \frac{2}{3}\delta_{ij}\frac{\partial \tilde{u}_k}{\partial x_k}\right) \tag{2}$$

$$\hat{q}_j = \frac{[\mu(\tilde{T}) + \mu_t]}{Pr}\frac{\partial \tilde{T}}{\partial x_j} \tag{3}$$

where the eddy viscosity μ_t must be expressed by a subgrid scale model. These equations are supplemented with the filtered equation of state, thanks to the reference Mach number M_0:

$$\bar{p} = (\bar{\rho}\tilde{T})\Big/\left(\gamma M_0^2\right) \tag{4}$$

Subgrid Scale Modeling

SMSM

Because of the large computational cost of the intended simulation, only one explicit subgrid scale model has been used for this study. The selective mixed scale model, developed by Sagaut and Lenormand, has been retained because it realizes a good compromise between accuracy, stability, and computational cost.[15] More particularly, the use of a selective function allows the handling of the transitional flows,[16] which is one of the keypoints of the present application. The eddy viscosity is given using a nonlinear combination of the filtered shear stress tensor, a characteristic length scale, the small-scale kinetic energy, and the selective function:

$$\mu_t = \bar{\rho} f_{\theta_0}(\theta) C_m \Delta \sqrt{0.5 S_{ij}(\tilde{u}) S_{ij}(\tilde{u})}\sqrt{K_c} \tag{5}$$

where the test field kinetic energy is evaluated as $K_c = \sqrt{[0.5(\tilde{u}_i)'(\tilde{u}_i)']}$. The test field $(\tilde{u}_i')$ is extracted from the resolved field $(\tilde{u}_i)' = \tilde{u}_i - \widehat{\tilde{u}_i}$ by employing a three-dimensional averaging test filter denoted by $\widehat{\tilde{u}_i} = A_i\{A_j[A_k(\tilde{u}_i)]\}$, with the following definition of A_l:

$$A_l(\phi) = 0.25\phi_{l-1} + 0.5\phi_l + 0.25\phi_{l+1} \tag{6}$$

The characteristic length scale Δ is given by the cell volume of the mesh, and the constant parameter $C_m = 0.06$ is derived in Ref. 17 from isotropic homogeneous turbulence flow cases. The selective function is defined by

$$f_{\theta_0}(\theta) = \begin{cases} 1 & \text{if} \quad \theta > \theta_0 = 10 \text{ deg} \\ \tan^4(\theta/2)/\tan^4(\theta_0/2) & \text{otherwise} \end{cases} \tag{7}$$

where θ is the angle between the filtered vorticity $\omega(\tilde{u})$ and the local averaged filtered vorticity $\omega(\hat{\tilde{u}})$.

MiLES

A simulation has been carried out with the MiLES approach,[11] which does not explicitly use a subgrid scale model based on

physical assumptions. As a consequence, the eddy viscosity in Eqs. (2) and (3) is set to zero. Thus the intrinsic dissipation of the numerical scheme is assumed to transfer the energy from the large scales to the small ones.

Numerical Method

General Description

The solver FLU3M, developed by ONERA, is based on a cell-centered finite volume technique and structured multiblock meshes. The viscous fluxes are discretized by a second-order-accurate centered scheme. For efficiency, an implicit time integration is employed to deal with the very small grid size encountered near the wall. Then a three-level backward differentiation formula is used to approximate the temporal derivative of Q_c in Eq. (1), leading to second-order accuracy. An approximate Newton method is employed to solve the nonlinear problem. At each iteration of this inner process, the inversion of the linear system relies on lower-upper symmetric Gauss–Seidel implicit method. More details about these numerical points are available in Ref. 18.

Euler Fluxes Discretization

Usually LES requires a high-order centered scheme for the Euler fluxes discretization (with spectral-like resolution) in order to minimize dispersive and dissipative numerical errors. However such scheme cannot be applied easily in complex geometry. Indeed, most of aerodynamic codes able to deal with such a geometry are based on finite volume technique in order to handle degenerated cell. Thus getting a high-order method becomes very time consuming because of the high-order quadrature needed to compute the fluxes along the cell boundaries. As several works (for instance, see Ref. 19) have shown that LES can be carried out with low-order centered scheme in case of sufficient mesh resolution, only a second-order-accurate scheme is employed in this study. But a special effort has been carried out to minimize the intrinsic dissipation of the scheme and its computational cost.

The AUSM + (P)[20,21] scheme, whose dissipation is proportional to the local fluid velocity, constitutes the basis of the discretization because it is well adapted to low-Mach-number boundary-layer simulations. However several modifications have been introduced to enhance its accuracy and computational cost. As we are not interested by the shock capturing properties of the scheme, simplified formulas are developed for this study to approximate the Euler fluxes of Eq. (1):

$$\bar{F}_1^{i+\frac{1}{2}} = U_1(Q_L + Q_R)/2 - |U_{\text{dis}}|(Q_R - Q_L)/2 + P \qquad (8)$$

where U_1 denotes the interface fluid velocity, L/R the left and right third-order MUSCL interpolation. The state vector Q is defined as $(\bar{\rho}, \bar{\rho}\tilde{u}_1, \bar{\rho}\tilde{u}_2, \bar{\rho}\tilde{u}_3, \bar{\rho}\tilde{E} + \bar{p})^t$, whereas the pressure term P is given by $[0, (\bar{p}_L + \bar{p}_R)/2, 0, 0, 0]$. The symbol U_{dis}, which indicates a local fluid velocity, characterizes the numerical dissipation acting on the velocity components. To enforce the pressure/velocity coupling in low-Mach-number zone, a pressure stabilization term is added to the interface fluid velocity as done by Rhie and Chow[22] for incompressible flow:

$$U_1 = (\tilde{u}_{1L} + \tilde{u}_{1R})/2 - c_2(\bar{p}_R - \bar{p}_L) \qquad (9)$$

where c_2 is a constant parameter. The parameter U_{dis} is defined as follows:

$$U_{\text{dis}} = \Phi \max(|\tilde{u}_{1L} + \tilde{u}_{1R}|/2, c_1) \qquad (10)$$

where c_1 is a constant parameter and Φ a sensor used to minimize the numerical dissipation. For an accuracy reason the values of c_1 and c_2 should be chosen as small as possible to minimize the numerical dissipation. For a stability reason these parameters cannot be smaller than a threshold value 0.04, which has been determined in Ref. 23. In the same spirit as the modification of the Jameson scheme proposed by F. Ducros (private communication, Centre Europeen de Recherche et de Formation Avancee en Calcul Scientifique, 2000), the present sensor Φ is a binary function, which only depends on the smoothness of the primitive variables $\psi = (\bar{\rho}, \tilde{u}_1, \tilde{u}_2, \tilde{u}_3, \bar{p})^t$. If no spurious oscillation is detected on ψ at cell i, Φ is equal to 0. Otherwise Φ is set to 1 at $i + \frac{1}{2}$ and $i - \frac{1}{2}$ interfaces. To detect a spurious oscillation and define exactly the sensor used in Eq. (10), the following functions are introduced:

$$\Delta_\phi^i = \begin{cases} -1 & \text{if} \quad (\phi_{i+2} - \phi_{i+1})(\phi_{i+1} - \phi_i) < 0 \\ 1 & \text{else} \end{cases}$$

$$W_{\psi_k} = \begin{cases} 1 & \text{if} \quad \Delta_{\psi_k}^i + \Delta_{\psi_k}^{i+1} < 0 \quad \text{or} \quad \Delta_{\psi_k}^i + \Delta_{\psi_k}^{i-1} < 0 \\ 0 & \text{else} \end{cases}$$

$$\Phi = \max\left(W_{\psi_k}\right) \qquad \text{for} \qquad k = 1, 5 \qquad (11)$$

However if the MiLES approach is retained as the SGS model, the sensor is set to one independently of primitive variables smoothness. In such case the energy transfer from the large scales to the small ones is achieved by the second term of Eq. (8).

Two-/Three-Dimensional Coupling Method

As LES of wall-bounded flow requires very small cells near the wall, it becomes essential to optimize the cell distribution in order to limit the total number of grid points. The specificity of external flows around infinite span body consists in the existence of a large zone, where the flow is laminar and two-dimensional. Thus three-dimensional computation can be limited to a zone close to the airfoil where the flow is turbulent, whereas two-dimensional laminar simulations are used for the far field (Fig. 1). As boundaries conditions are treated through ghost cells, the two-/three-dimensional coupling is realized by the following definitions of ghost cell data:

$$Q_c^{2D}(x, y) = L_z^{-1} \int_0^{Lz} Q_c^{3D}(x, y, z)\, \mathrm{d}z$$

$$Q_c^{3D}(x, y, z) = Q_c^{2D}(x, y) \qquad (12)$$

where L_z denotes the spanwise extent of the computational domain. If the boundary between two- and three-dimensional blocks is located too close from turbulent zones, the flow variables in the three-dimensional block are subject to an implicit spanwise filtering. Therefore the extent of the three-dimensional zone in the direction normal to the wall must be chosen carefully to realize a good compromise between efficiency and accuracy. For flow over airfoil, the turbulent boundary-layer thickness, which grows from the leading edge to the trailing edge, is often less than 10% of the chord. Thus the two-/three-dimensional technique can easily reduce the total number of grid points by a factor two, especially if several three-dimensional blocks with different extents in the direction normal to the wall are used to fit the turbulent boundary-layer topology.

Numerical Results

Airfoil Configuration

The A-Airfoil designed by Aérospatiale has been retained for this study. Measurements have been carried out at ONERA in two different wind tunnels[24] for a wide range of Reynolds numbers, Mach numbers, and angles of incidence. Skin friction, surface pressure, and laser Doppler velocimetry measurements of both velocity profiles and turbulence intensities are available. This work focuses on the simulation of the near-stall configuration: the Reynolds number, based on the upstream velocity ($u_\infty = 50$ ms^{-1}) and the chord ($c = 0.6$ m), is equal to 2.1×10^6, whereas the angle of attack and upstream Mach number are set to 13.3 deg and 0.15, respectively. Transition was triggered on the pressure side at $x/c = 0.3$. Because of the strong adverse pressure gradient, transition occurs naturally on the suction side: there is a laminar separation bubble, which leads to a turbulent reattachment near $x/c = 0.12$. After this position the development of the turbulent boundary layer is marked by the presence of a second separation zone, which occurs between $x/c \approx 0.82$ and the blunt trailing edge. (Its thickness is nearly equal to 0.5% of the chord.) This flow complexity renders the test case very challenging for the CFD community because previous Reynolds-averaged Navier–Stokes (RANS)[25] and LES (Ref. 5 and manuscript in preparation) simulations failed to predict correctly some important flow features, especially the separation zone at the trailing edge.

Computational Setup

As our purpose is to highlight the possibilities and limitations of LES for such flows, four C-H meshes have been used to evaluate the simulation sensitiveness to different spatial resolution parameters. In the (x, y) plan (see Fig. 1), all of the designed meshes have a computational domain limit located at approximately 10 chords of the airfoil. The main characteristics of the meshes are summarized in Table 1. The rows Wake, PS, SS, N_2, N_3, and $Nb \cdot$ pts correspond to the number of cells in the wake, on the pressure side, on the suction side, in the direction normal to the wall, and in the spanwise direction and the total number of cells, respectively.

For the $M4$ mesh identical to Weber's one,[5] the blunt trailing edge is replaced by a sharp one for sake of simplicity. If the wall normal resolution is sufficient ($\Delta y^+ \approx 2$), the average streamwise and spanwise resolution on the suction side are very crude for LES ($\Delta x^+ \approx 800$ and $\Delta z^+ \approx 200$, respectively). Thus this mesh allows us to illustrate the validity of strongly underresolved LES for complex flow.

The $M1, \ldots, M3$ grids have been designed to obtain a classical LES resolution. In the (x, y) plan all meshes are identical. The blunt trailing edge is discretized through a $96 \times 40 \times N_3$ H-H block. As the thickness of the suction side boundary layer is one order of magnitude larger than those of the pressure side, it is assumed that the error committed in the pressure side has little influence on the global solution accuracy. Thus pressure-side boundary layer is assumed to remain laminar. Therefore only 430 cells are located on this side, and a two-dimensional block is used from $x/c = 0.01$ to 0.98 to limit the number of points (Fig. 2). In the same way, two three-dimensional blocks, with wall normal extent close to $0.015c$ and $0.1c$, respectively, are used on the suction side to fit the growth of the boundary layer. The first block, with 38 cells in the wall normal direction, is located between $x/c = 0.01$ and 0.38. The second one goes from $x/c = 0.38$ to the limit of the computational domain, with 48 cells in the wall normal direction. The Mk grids ($k = 1, 3$) differ only by their spanwise characteristics. On the one hand, the $M2$ and $M3$ meshes, with spanwise extent of $0.012c$ and $0.005c$ respectively, allow the checking of the influence of this parameter because their spanwise resolution are equal. On the other hand, the $M1$ and $M3$ meshes highlight the effect of the spanwise resolution. Figure 3 displays the mesh resolution of $M3$ in wall unit. (This unit is evaluated with the mean skin-friction coefficient of the $M3$ simulation, which is in good agreement with experimental measurement as illustrated by Fig. 4.) The mesh resolution usually required by LES of wall-bounded flow ($\Delta y^+ \approx 2$, $\Delta z^+ \approx 20$, $\Delta x^+ \approx 100$) is almost reached everywhere. The problem of these grids concerns the limited spanwise extent ($\leq 0.012c$), which could happen to be too short near the trailing edge. Because no experimental data dealing with the spanwise correlation length are available, the spanwise extent of the domain will be chosen empirically. However available supercomputer and current numerical method do not allow handling of the larger domain with LES resolution.

Table 1 Mesh characteristics

Mesh	Wake	PS	SS	N_2	N_3	L_z/c	Two-/three-dimensional	$Nb \cdot$ pts
$M1$	96	430	2048	90	30	1.2%	Yes	3.2×10^6
$M2$	96	430	2048	90	30	0.5%	Yes	3.2×10^6
$M3$	96	430	2048	90	72	1.2%	Yes	7.2×10^6
$M4$	57	192	192	64	32	3%	No	10^6

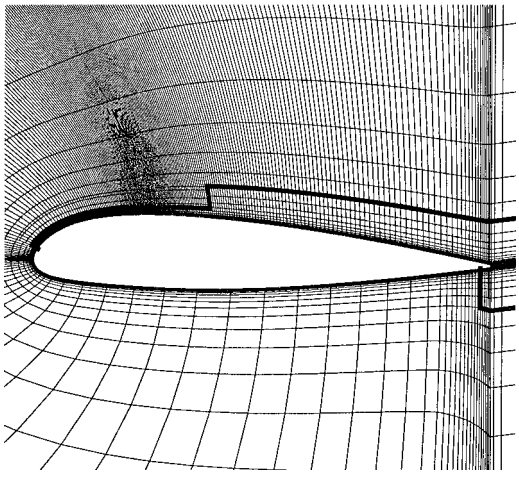

Fig. 2 ***Mk*** **($k = 1, 3$) mesh in the (x, y) plan (10% of the nodes is represented in the streamwise direction and 50% in the wall normal direction). The thick line represents the limit between two- and three-dimensional zones.**

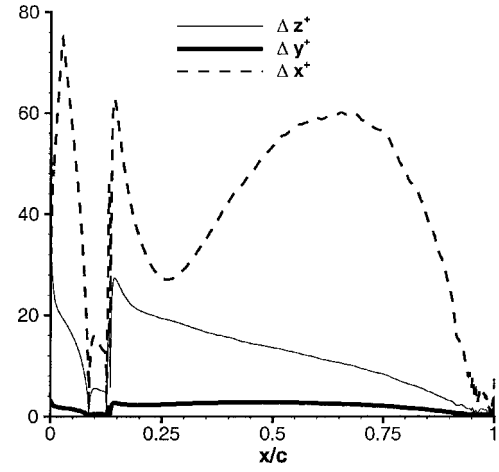

Fig. 3 ***M3*** **mesh: evolution of the mesh resolution on the suction side in wall unit.**

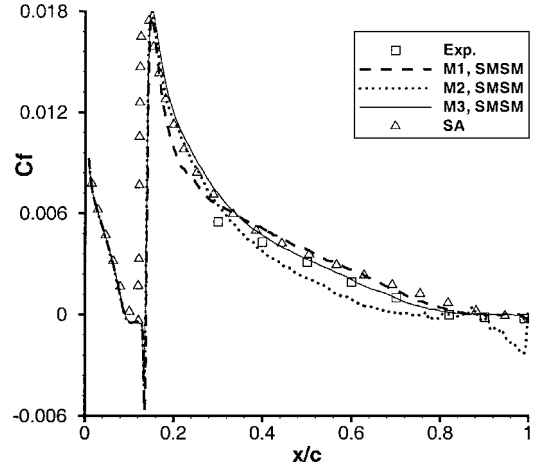

Fig. 4 Effect of spanwise mesh properties on the mean skin-friction coefficient C_f.

All simulations are based on the flow parameters of the configuration described in the preceding section. They are obtained by using no-slip and periodic conditions at the wall and in the spanwise direction, respectively. Nonreflecting characteristic boundary conditions are applied for the far field. Moreover, a RANS simulation using Spalart–Allmaras model[26,27] provides an initial flow solution. For these simulations the turbulent viscosity is set to zero if $x/c \leq 0.12$, which corresponds to the experimental location of the turbulence onset. The time step is fixed at $\Delta t = 3.3 \times 10^{-5} c/u_\infty$, implying a maximal Courant–Friedrichs–Lewy number close to 16. For the $M1$ simulation, around six time units are necessary to get a well-established unsteady solution from the initial steady RANS solution . To reduce the CPU time, the $M1$ flowfield is retained as initial condition for the $M2$ and $M3$ simulations, limiting the initial transient to 1.5 time units. For average quantities the averaging procedure is performed in the homogeneous spanwise direction and in time over a period of $2.4c/u_\infty$. The simulations are carried out on a single processor of NEC SX5, and the code is running approximately at 4Gflops (for a crest speed of 8Gflops). Almost 366 CPU

hours are needed to performed the time integration over a period of $2.4c/u_\infty$ on the largest grid $M3$.

Results Analysis

To discard inaccurate results, Figs. 5 and 6 depict the mean pressure coefficient $C_p = 2(p - p_\infty)/\rho u_\infty^2$ and the mean skin-friction coefficient $C_f = 2\tau_w/\rho u_\infty^2$ (τ_w represents the wall shear stress) obtained with the different SGS modelings on the $M1$ and $M4$ grids. Figure 5 clearly shows that the mesh resolution in the (x, y) plane has a deeper impact on the solution accuracy of C_p than the SGS modeling. Indeed, MiLES and SMSM results are nearly identical on both meshes, whereas $M1$ and $M4$ results strongly differ. Results associated with the $M4$ meshes are characterized by a strong overestimation of the suction peak value, and no plateau is detected near the trailing edge, indicating that no separation occurs. The C_p distributions on $M1$ mesh are in very good agreement with experimental data and more particularly the SMSM results. Indeed, both the plateau and suction peak values are well predicted, whereas the sharp gradient near $x/c = 0.12$ underlines the presence of laminar separation bubble and turbulent reattachment, as mentioned in the experimental report.[24] Concerning the MiLES solution, the C_p distribution begins to slightly differ from experimental data at $x/c = 0.8$ because no plateau is detected. This indicates that no separation occurs with the implicit SGS modeling, which is confirmed by the value of the skin-friction coefficient on Fig. 6. As this variable is strongly related to viscous effects, both the SGS modeling and mesh resolution have a significant effect on the suction side C_f distribution. The $M4$ simulations lead to earlier transition than the $M1$ ones independently of the SGS modeling, but both models yield unsatisfactory behaviors of the C_f distribution. Therefore, for brevity the results of $M4$ simulations are not presented hereafter. As the C_p distributions on $M1, \ldots, M3$ meshes are almost identical between $x/c = 0$ and 0.6 on the both sides of the airfoil, Fig. 7 shows only the influence of spanwise mesh properties near the trailing edge. The RANS results obtained with the Spalart–Allmaras (SA) model on the same (x, y) mesh are presented to put the LES results in perspective. The size and intensity of the separation zone can be estimated by the value and extent of the plateau. No separation occurs with the SA simulation. For LES results it appears that both the spanwise extent and resolution have a significant impact on this flow region. Indeed, $M3$ simulation exhibits a very good agreement with experimental data. But the use of smaller spanwise extent in the $M2$ simulation leads to a large overestimation of both the size and intensity of the separation, whereas the use of coarser spanwise resolution in the $M1$ simulation implies a too weak separation. It seems that the reduced spanwise extent of the $M2$ mesh leads to a nearly two-dimensional flow at the trailing edge, characterized by the presence of spurious intense vortices, which scale with the boundary-layer thickness. As mentioned in Ref. 28, the large timescale of these eddies decreases the rate of statistical convergence, leading to the small irregularities observed in the suction side C_p distribution.

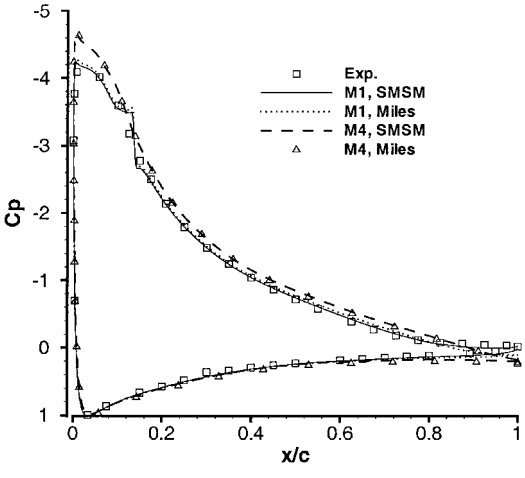

Fig. 5 Effect of SGS modeling and (x, y) mesh resolution on the mean pressure coefficient C_p.

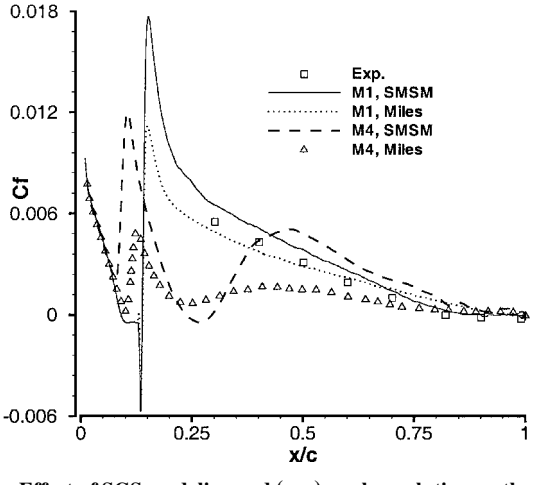

Fig. 6 Effect of SGS modeling and (x, y) mesh resolution on the mean skin-friction coefficient C_f.

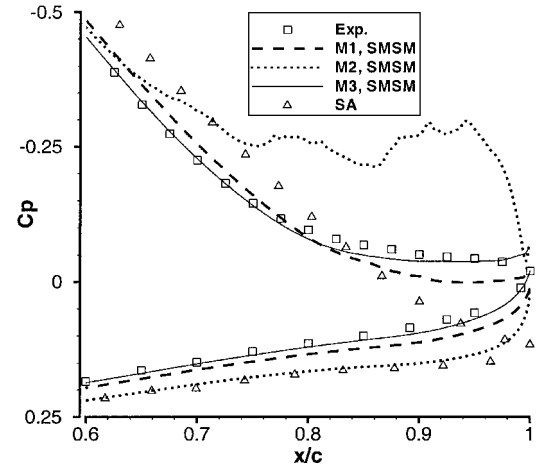

Fig. 7 Effect of spanwise mesh properties on the mean pressure coefficient C_p near the trailing edge.

Figure 4 shows the mean C_f distribution on the suction side. It appears that the separation bubble, located between $x/c = 0.09$ and 0.13, is not affected by the use of the different $M1, \ldots, M3$ meshes. Moreover the characteristic features of a laminar separation bubble described by Alam and Sandham[29] are well recovered: they are a flat distribution up to $x/c = 0.12$ corresponding to the dead-air region and a large negative peak associated to the reverse flow vortex. This good physical behavior can be related to the streamwise mesh resolution because around 110 mesh points are located in the separation zone, followed by 40 points up to the positive peak as a result of the turbulent reattachment at $x/c = 0.15$. After this position the $M1, \ldots, M3$ solutions start to differentiate. As for the C_p distribution, the $M3$ simulation allows a very good agreement with experimental skin-friction measurements. Indeed the largest error, located at $x/c = 0.3$, is less than 28%. The experimental value at this position is not very accurate because the experimental evaluation of the skin friction relies on the hypothesis of the existence of a logarithmic layer, whereas the boundary layer is still in nonequilibrium.[24] Therefore the commited error is less than 6% for the most reliable measurements (between $x/c = 0.5$ and 0.7). The use of reduced spanwise extent in the $M2$ simulation does not modify the friction coefficient up to $x/c = 0.25$. But after this position the spanwise blockage of the turbulent structures implies an undershoot of C_f, leading to a too important reverse flow at the trailing edge. The use of larger spanwise resolution in the $M1$ simulation modifies the skin-friction coefficient in a more complex way. Two zones could be distinguished: up to $x/c = 0.35$ the unsufficient resolution does not allow to represent accurately the turbulent structures, leading to an undershoot of C_f; after this location C_f is overshooted, but the slope of $M3$ results is almost recovered, which might indicate that

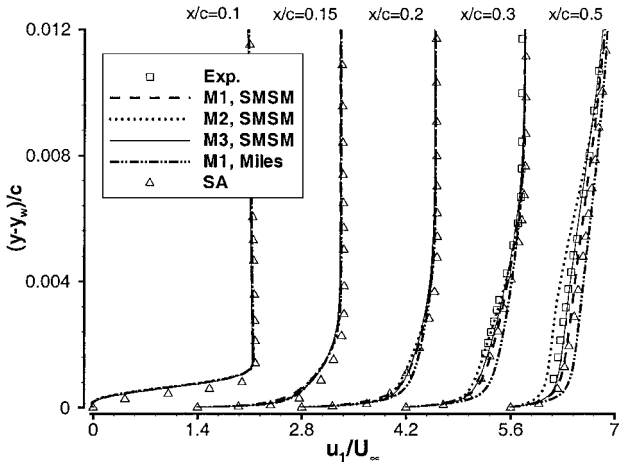

Fig. 8 Mean streamwise velocity profiles in function of normalized wall normal distance; individual profiles are separated by a horizontal offset of 1.4 with the corresponding zero lines located at 0, 1.4, . . . , 7.

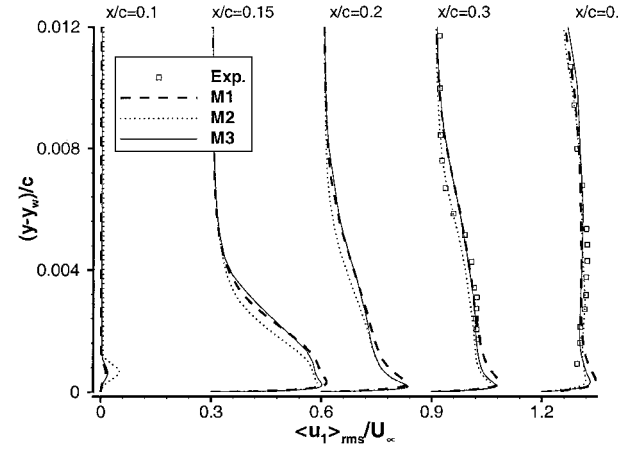

Fig. 10 Profile of the rms streamwise velocity fluctuations obtained with the SMSM model; individual profiles are separated by a horizontal offset of 0.3 with the corresponding zero lines located at 0, 0.3, . . . , 1.2.

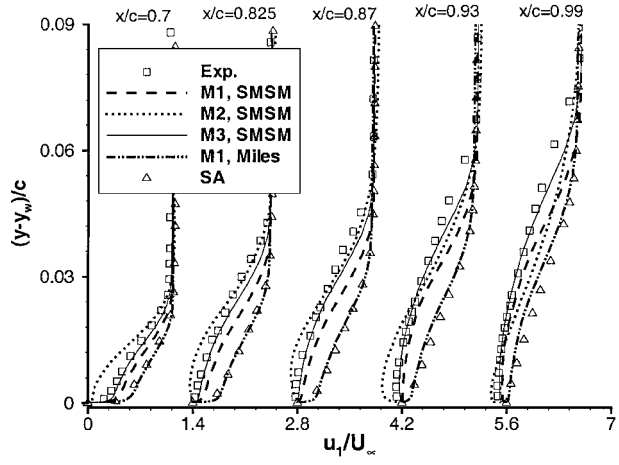

Fig. 9 Mean streamwise velocity profiles in function of normalized wall normal distance; individual profiles are separated by horizontal offset of 1.4 with the corresponding zero lines located at 0, 1.4, . . . ,7.

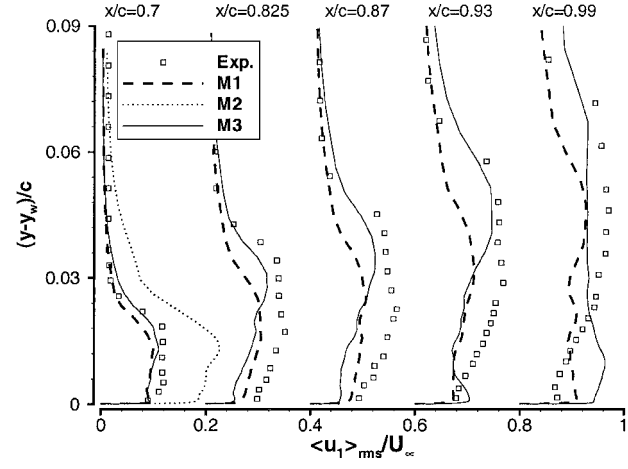

Fig. 11 Profile of the rms streamwise velocity fluctuations obtained with the SMSM model; individual profiles are separated by a horizontal offset of 0.2 with the corresponding zero lines located at 0, 0.2, . . . , 1.

the resolution is sufficient in this zone. For the RANS simulation the result is quite satisfying in the transition zone, but the friction coefficient is overestimated after $x/c = 0.5$.

Figures 8 and 9 compare computational and experimental (when available) mean streamwise velocity profiles in the wall-normal coordinate system located between $x/c = 0.1$ and 0.99. It appears that up to $x/c = 0.2$ the profiles are not sensitive to the use of the different $M1, \ldots, M3$ meshes. Once again, the $M3$ simulation is in very good agreement with experimental profiles because the growth and shape of the boundary layer are well recovered at all locations. The use of coarser spanwise resolution in the $M1$ simulation leads to fuller profiles in the near-wall region, which delays the separation in the trailing-edge zone. This phenomenon is all the more pronounced as the MiLES model is used. In such a case the results are nearly identical to RANS ones, and no separation occurs at the trailing edge. In the contrary, larger shape factors are obtained with the shorter spanwise extent in the $M2$ simulation, leading to a too early separation around $x/c = 0.75$.

The rms streamwise velocity profiles in the wall-normal coordinate system are plotted in function of the normalized wall normal distance in Figs. 10 and 11. For clarity, $M2$ results are not shown in Fig. 11 at positions $x/c = 0.825$–0.99. Indeed, the too limited spanwise extent generates very intense nonphysical fluctuations typical of two-dimensional simulations,[30] illustrated by the overestimations of 100% at $x/c = 0.7$. Farther downstream, these overshoots can reach 250%, prohibiting a clear representation of all results on the same figure. From $x/c = 0.1$ to 0.7 results of the different simulations are very close and in quite good agreement with the experimental data (if available). The small fluctuations detected at $x/c = 0.1$ on Fig. 10, especially for the $M2$ simulation, indicate that the dead-air region slightly oscillates in the laminar bubble. After this position the intense fluctuation (close to 30% of u_∞) occurring at $x/c = 0.15$ in the turbulent reattachment zone relaxes slowly to a value typical of turbulent boundary layer near equilibrium at $x/c = 0.5$. The well-known near-wall peaks are slightly larger with the $M1$ simulation, but no experimental measurement is available so close to the wall, preventing the validation of this point. If $M1$ and $M3$ results are still in quite good agreement with experimental data at $x/c = 0.7$, significant discrepancies occur downstream in the separated region, especially on the $M1$ mesh. This can be caused by both simulation and measurement errors. On the one hand, the spanwise extent equal to $0.012c$ becomes more and more unadapted to the boundary-layer thickness, which is close to 0.1 at $x/c = 0.99$. On the other hand, the accuracy of rms turbulence intensity measurements deteriorates when the local mean velocity has the same order of magnitude,[24] as in the trailing-edge separation zone. Another point is that large-scale fluctuations caused by the presence of sidewalls might be suspected in the wind tunnel.

Figure 12 depicts a view of a pressure fluctuation isosurface in the transitional zone of the $M1$ simulation. Contrary to the results of Weber and Ducros[5] characterized by a transitional zone spreading on two or three cells caused by insufficient mesh resolution, the present simulations on $M1, \ldots, M3$ allow the recovering of a classical transition process: development of two-dimensional waves, followed by the formation of three-dimensional structures. As no artificial trip is used in the simulations, the numerical noise replaces the

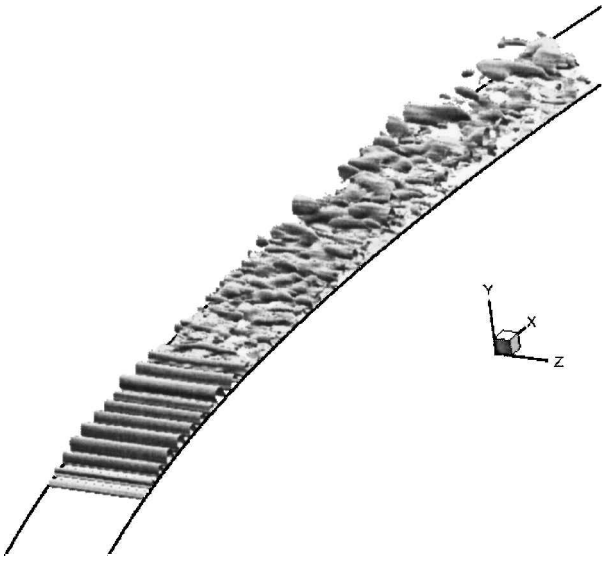

Fig. 12 Three-dimensional view of pressure fluctuation isosurface in the transitional zone on the *M*1 mesh.

action of freestream turbulence or surface roughness, which generates three-dimensional structures in practical application.

Conclusions

To highlight the possibilities of LES in an aeronautical context, LES have been carried out for a flow over an airfoil near stall at a chord Reynolds number of 2.1×10^6. This configuration leads to a complex flow because laminar bubble, turbulent reattachment, and separation near the trailing edge occur successively in the suction-side boundary layer. To keep the simulations in the validity domain of current state of the art in LES, both local mesh-refinement technology and a new discretization of the convective fluxes have been proposed, allowing the use of both sufficient mesh resolution on the available supercomputer and low dissipative scheme for such complex flow.

Influence of mesh resolutions and SGS modelings have been assessed. For a same mesh resolution it appears that explicit SGS modeling performs better than the MiLES model used in this study if turbulent structures are sufficiently well described by the grid. But in case of a too coarse grid resolution, explicit SGS modeling becomes as unadapted as the implicit MiLES approach. The effects of both spanwise extent and resolution have been investigated, showing a great influence of these parameters. With the use of the largest extent and finest resolution, the computed mean and fluctuating velocity profiles compare reasonably well with experimental measurements, which constitutes to the authors' knowledge the first satisfying LES of this complex flow.

Acknowledgments

This work is a part of the LESFOIL project (Project BRPR-CT97-0565), financed by the Brite-Euram Programme. The authors acknowledge all European consortium members for interesting discussion during the last years. S. Daux, O. Nyst, and P. Guillen are warmly acknowledged for preliminary studies dealing with the MiLES approach, D. Blaise for helpful discussions about boundary layers, and S. Deck for the RANS simulation.

References

[1]Manoha, E., Troff, B., and Sagaut, P., "Trailing-Edge Noise Prediction Using Large Eddy Simulation and Acoustic Analogy," *AIAA Journal*, Vol. 38, No. 4, 2000, pp. 575–583.

[2]Wang, M., and Moin, P., "Computation of Trailing-Edge Flow and Noise Using Large Eddy Simulation," *AIAA Journal*, Vol. 38, No. 12, 2000, pp. 2201–2209.

[3]Jansen, K., "Unstructured-Grid Large-Eddy Simulation of Flow over an Airfoil," *Annual Research Brief*, Center for Turbulence Research, NASA Ames Research Center/Stanford Univ., Stanford, CA, 1994, pp. 161–175.

[4]Kaltenbach, H. J., and Choi, H., "Large-Eddy Simulation of Flow over an Airfoil on Structured Meshes," *Annual Research Brief*, Center for Turbulence Research, NASA Ames Research Center/Stanford Univ., Stanford, CA, 1995, pp. 51–61.

[5]Weber, C., and Ducros, F., "Large Eddy and Reynolds-Averaged Navier–Stokes Simulations of Turbulent Flow over an Airfoil," *International Journal of Computational Fluid Dynamics*, Vol 13, 2000, pp. 327–355.

[6]Nicoud, F., Bagett, J. S., Moin, P., and Cabot, W., "LES Wall-Modeling Based on Sub-Optimal Control Theory and Linear Stochastic Estimation," *Physics of Fluids*, Vol. 13, No. 10, 2001, pp. 2968–2984.

[7]Kravchenko, A. G., Moin, P., and Shariff, K., "B-Spline Method and Zonal Grids for Simulations of Complex Turbulent Flows," *Journal of Computational Physics*, Vol. 151, No. 2, 1999, pp. 757–789.

[8]Fröhlich, J., Rodi, W., Kessler, Ph., Parpais, S., Bertoglio, J. P., and Laurence, D., "LES of Flow Around Circular Cylinders on Structured and Unstructured Grids," *Note on Numerical Fluid Mechanics*, edited by E. H. Hirschel, Vol. 66, Vieweg, Brunswick, Germany, 1998, pp. 319–338.

[9]Quéméré, P., Sagaut, P., and Couailler, V., "A New Multi-Domain/Multi-Resolution Method for Large Eddy Simulation," *International Journal for Numerical Methods in Fluids*, Vol. 36, No. 4, 2001, pp. 391–416.

[10]Pascarelli, A., Piomelli, U., and Candler, V., "Multi-Block Large Eddy Simulations of Turbulent Boundary Layers," *Journal of Computational Physics*, Vol. 157, No. 1, 2000, pp. 256–279.

[11]Boris, J. P., Grinstein, F. F., Oran, E. S., and Kolbe, R. L., "New Insights into Large Eddy Simulation," *Fluid Dynamic Research*, Vol. 10, 1992, pp. 199–228.

[12]Fureby, C., and Grinstein, F., "Towards Large Eddy Simulation of Flows in Complex Geometries," AIAA Paper 98-2806, 1998.

[13]Garnier, E., Mossi, M., Sagaut, P., Comte, P., and Deville, M., "On the Use of Shock Capturing Schemes for Large Eddy Simulation," *Journal of Computational Physics*, Vol. 153, No. 2, 1999, pp. 273–311.

[14]Ducros, F., Ferrand, V., Nicoud, F., Weber, C., Darracq, D., Gacherieu, C., and Poinsot, T., "Large Eddy Simulation of Shock/Turbulence Interaction," *Journal of Computational Physics*, Vol. 152, No. 2, 1999, pp. 517–549.

[15]Lenormand, E., Sagaut, P., Ta Phuoc, L., and Comte, P., "Subgrid-Scale Models for Large-Eddy Simulation of Compressible Wall Bounded Flows," *AIAA Journal*, Vol. 38, No. 8, 2000, pp. 1340–1350.

[16]David, E., "Modélisation des Écoulements Compressibles et Hypersoniques: une Approche Instationnaire," Ph.D. Dissertation, Mechanical Dept., l'Inst. National Polytechnique de Grenoble, France, Oct. 1999.

[17]Sagaut, P., *Large-Eddy Simulation of Incompressible Flows. An Introduction*, Springer-Verlag, Berlin, 2001.

[18]Péchier, M., Guillen, P., and Gayzac, R., "Magnus Effect over Finned Projectiles," *Journal of Spacecraft and Rockets*, Vol. 38, No. 4, 2001, pp. 542–549.

[19]Wu, X., Jacobs, R., Hunt, J., and Durbin, P., "Simulation of Boundary Layer Transition Induced by Periodically Passing Wake," *Journal of Fluid Mechanics*, Vol. 398, 1999, pp. 109–153.

[20]Edwards, J. R., and Liou, M. S., "Low-Diffusion Flux-Splitting Methods for Flows at All Speeds," *AIAA Journal*, Vol. 36, No. 9, 1998, pp. 1610–1617.

[21]Mary, I., Sagaut, P., and Deville, M., "An Algorithm for Unsteady Viscous Flows at All Speeds," *International Journal for Numerical Methods in Fluids*, Vol. 34, No. 5, 2000, pp. 371–401.

[22]Rhie, C. M., and Chow, W. L., "Numerical Study of the Turbulent Flow past an Airfoil with Trailing Edge Separation," *AIAA Journal*, Vol. 21, No. 11, 1983, pp. 1525–1532.

[23]Mary, I., "Méthode de Newton Approchée pour le Calcul d'Écoulements Instationnaires Comportant des Zones à Très Faibles Nombres de Mach," Ph.D. Dissertation, Mechanical Dept., Univ. Paris XI, Paris, Oct. 1999.

[24]Gleyzes, C., "Opération Décrochage- Résultats des Essais à la Soufflerie F2," ONERA, Technical Rept. RT-OA 19/5025, Chatillon, France, June 1988.

[25]Haase, W., Chaput, E., Elsholz, E., Leschziner, M., and Müler, U. (eds.), "ECARP-European Computational Aerodynamic Research Project: Validation of CFD Codes and Assessment of Turbulence Models," *Notes on Numerical Fluids Mechanics*, Vol. 58, Vieweg, Brunswick, Germany, 1997, pp. 325–346.

[26]Spalart, P., and Allmaras, S., "A One-Equation Turbulence Model for Aerodynamic Flows," *La Recherche Aérospatiale*, Vol. 1, 1994, pp. 5–21.

[27]Deck, S., Duveau, P., d'Espiney, P., and Guillen, P., "Development and Application of Spalart-Allmaras One-Equation Turbulence Model to Three-Dimensional Supersonic Complex Configurations," *Aerospace Science and Technology* (to be published).

[28]Na, Y., and Moin, P., "Direct Numerical Simulation of a Separated Turbulent Boundary Layer," *Journal of Fluid Mechanics*, Vol. 374, 1998, pp. 379–405.

[29]Alam, M., and Sandham, N. D., "Direct Numerical Simulation of Short Laminar Separation Bubbles with Turbulent Reattachment," *Journal of Fluid Mechanics*, Vol. 410, 2000, pp. 1–28.

[30]Sohankar, A., Norberg, C., and Davidson, L., "Simulation of Three-Dimensional Flow Around a Square Cylinder at Moderate Reynolds Numbers," *Physics of Fluids*, Vol. 11, No. 2, 1999, pp. 288–306.

R. M. C. So
Associate Editor